

Article

ADRC Control System of PMLSM Based on Novel Non-Singular Terminal Sliding Mode Observer

Zheng Li *, Zihao Zhang, Jinsong Wang, Shaohua Wang, Xuotong Chen and Hexu Sun *

School of Electrical Engineering, Hebei University of Science and Technology, Shijiazhuang 050018, China; zhangzihao@stu.hebust.edu.cn (Z.Z.); wangjingsong@stu.hebust.edu.cn (J.W.); wangshaohua@stu.hebust.edu.cn (S.W.); chenxuotong@stu.hebust.edu.cn (X.C.)

* Correspondence: lizheng@hebust.edu.cn (Z.L.); hxsun@hebust.edu.cn (H.S.); Tel.: +86-311-8166-8722 (H.S.)

Abstract: In an attempt to solve the problem of the many parameters of the traditional active disturbance rejection controller (ADRC) and to accurately estimate the mover position and speed required by a permanent magnet synchronous linear motor (PMLSM) system, an improved ADRC and a novel nonsingular fast terminal sliding mode observer (NFTSMO) are proposed. Firstly, the traditional first-order ADRC is simplified, the tracking differentiator (TD) module is removed, and the direct error is used to replace the nonlinear function in the extended state observer (ESO) and nonlinear state error feedback (NLSEF) module. Based on the traditional NFTSMO, the smooth back electromotive force (EMF) is obtained by adding the TD to reduce the phase delay caused by the low-pass filter in the traditional sliding mode observer (SMO), and the actuator position and speed information are modulated from the observed back EMF based on the principle of a phase-locked loop (PLL). Simulation and experiments show that this method not only simplifies the system structure of PMLSM but also optimizes many parameters in ADRC while retaining the original excellent performance. Compared with the traditional NFTSMO, the improved NFTSMO enhances the observation accuracy, reduces the chattering phenomenon of the system, and improves the robustness of the system.

Keywords: permanent magnet synchronous linear motor; active disturbance rejection control policy; non-singular terminal sliding mode observer; tracking differentiator



Citation: Li, Z.; Zhang, Z.; Wang, J.; Wang, S.; Chen, X.; Sun, H. ADRC Control System of PMLSM Based on Novel Non-Singular Terminal Sliding Mode Observer. *Energies* **2022**, *15*, 3720. <https://doi.org/10.3390/en15103720>

Academic Editor: Mario Marchesoni

Received: 3 April 2022

Accepted: 17 May 2022

Published: 19 May 2022

Publisher's Note: MDPI stays neutral with regard to jurisdictional claims in published maps and institutional affiliations.



Copyright: © 2022 by the authors. Licensee MDPI, Basel, Switzerland. This article is an open access article distributed under the terms and conditions of the Creative Commons Attribution (CC BY) license (<https://creativecommons.org/licenses/by/4.0/>).

1. Introduction

PMLSM has the advantages of high precision, high speed, and a fast response and is widely used in aerospace, the arms industry, intelligent robots, high-precision lathe, and other fields because of its tiny footprint, high efficiency, strong robustness, and low requirements for the equipment environment [1–3]. Compared with permanent magnet synchronous motors (PMSM), PMLSM can convert input electrical energy into mechanical energy that drives motion without conversion [4]. The structure of the motor system without a conversion device significantly decreases the system error and improves the accuracy of the system.

Servo control is significant to the PMLSM control system. During the operation of PMLSM, it is often affected by many disturbance factors such as air resistance, groove force, end effect, and internal parameters so that the operation difficulty of the linear motor increases and the control accuracy decreases [5]. The conventional solution is to add the traditional PID control technology to the system; the control technology has good robustness, a short calculation time, the overall structure is simple, they are often applied to the control accuracy, and the response speed does not have high requirements [6]. In the subsequent studies, model reference adaptive control [7], sliding mode variable structure control, and other control methods based on modern control theory were proposed, which improved the control accuracy but also resulted in a jitter phenomenon and slow system

response [8]. ADRC technology is characterized by clear overall structure classification, a simple and convenient algorithm, fast system response, high control accuracy, and effective improvement of multiple disturbance factors of the controlled object model with high robustness [9]. ADRC technology can also estimate the system disturbance factors according to the real-time information on the system, and it has a good estimation effect, especially for the multiple disturbance factors inside and outside the control system [10]. The main working principle of ADRC technology is to compensate the input of the closed-loop system with the estimated disturbance value in real-time and transform a relatively complex control system into a relatively simple control system so that the closed-loop control system can obtain excellent control performance while simplifying the system structure. This effectively improves the control performance and operation accuracy of the system [11].

In the PMLSM control system, a mechanical sensor is usually added to the linear motor to output the speed and position information on the actuator, such as adding a resolver and a photoelectric encoder [12]. However, the addition of mechanical sensors also increases the occupied space and weight of the linear motor, which affects the accuracy and increases the inertia of the motor bearing, thus bringing additional load [13]. To solve these problems, the sensorless control strategy has become an important method of the linear motor. Sensorless motor control strategies are mainly divided into neural network algorithms [14], high-frequency injection mode [15], SMO, etc. The SMO method has strong stability against multiple internal and external disturbances inside the motor. It has a simple overall structure and a wide range of applications and is usually used in sensorless control strategies for motors [16]. However, SMO may also cause frequency chattering in the control system due to the discontinuity of the switching function, as well as the extensive calculations involved in installing a low-pass filter (LPF) and phase compensation [17]. Sinusoidal saturation function, higher-order sliding mode theory, and terminal sliding mode theory are often introduced to solve the above problems, which can reduce the chattering phenomenon and improve robustness [18]. The NFTSMO adopts the method of combining nonlinear functions and linear functions with non-singular fast terminal sliding mode surfaces to quickly design a terminal sliding mode control strategy, which realizes the rapid convergence of errors in different stages and reduces the chattering phenomenon. The traditional SMO has the advantages of solid robustness, fast response speed, and high steady-state tracking performance [19,20].

This paper takes the active disturbance rejection control strategy of PMLSM as the research object. Among them, the speed and current in the system are controlled by ADRC, and it is simplified based on the traditional first-order ADRC control system to reduce the multiple disturbance factors in the system. Meanwhile, based on the traditional NFTSMO, a novel NFTSMO is proposed based on the terminal sliding mode theory and tracking differentiator, and the PLL structure is used to extract the position information of the actuator, which can effectively reduce the chattering phenomenon and improve the observation accuracy. Through simulation analysis and experimental verification, the control system simplifies the traditional structure, enhances robustness and observation accuracy, and has excellent tracking performance.

2. Mathematical Model of PMLSM

The structure diagram of the PMLSM used in this article is shown in Figure 1.

PMLSM is a nonlinear system with many variables. It is assumed that the armature reaction magnetic field and excitation magnetic field in the linear motor are distributed sinusoidal, and on this basis, the hysteresis loss, eddy current loss, magnetic saturation effect, and nonlinear friction of the motor are ignored. Thus, the voltage equation of PMLSM under the d-q axis of the synchronous rotation coordinate system can be obtained as

$$\begin{cases} u_d(t) = R_s i_d + L_d \frac{di_d}{dt} - \frac{\pi}{\tau} v \psi_q \\ u_q(t) = R_s i_q + L_q \frac{di_q}{dt} + \frac{\pi}{\tau} v \psi_d \end{cases} \quad (1)$$

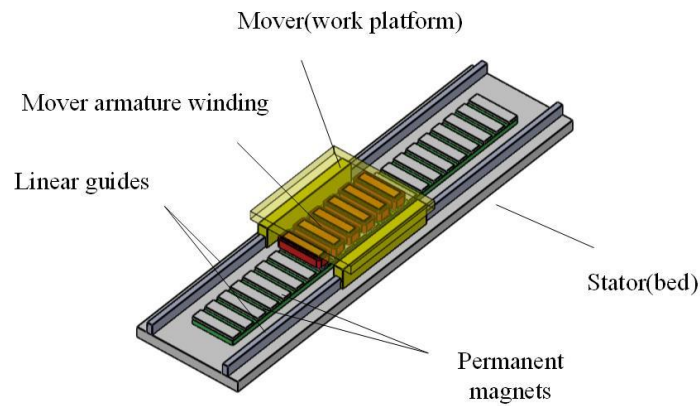


Figure 1. Structure diagram of PMLSM.

In the above formula, R_s is the stator resistance; τ is the pole distance of PMLSM; v is the running speed of the linear motor; $[u_d \ u_q]^T$ are the stator voltages of the d-axis and q-axis, respectively; $[i_d \ i_q]^T$ are the stator current of the d-axis and q-axis, respectively; $[L_d \ L_q]^T$ are the inductance components of the d-axis and q-axis, respectively; $L_d = L_q = L$ in the linear motor adopted this time. The stator flux equation is

$$\begin{cases} \psi_d = Li_d + \psi_f \\ \psi_q = Li_q \end{cases} \quad (2)$$

where ψ_f is the permanent magnet flux. According to Formula (1), the current state equation of the PMLSM is

$$\begin{cases} \frac{di_d}{dt} = -\frac{R_s}{L}i_d + \frac{\pi L_q}{\tau L}vi_q + \frac{u_d}{L} \\ \frac{di_q}{dt} = -\frac{R_s}{L}i_q - \frac{\pi L_d}{\tau L}vi_d + \frac{u_q}{L} - \frac{\pi\psi_f}{\tau L}v \end{cases} \quad (3)$$

The electromagnetic thrust equation of PMLSM is

$$F_{em} = p_n \frac{3\pi}{2\tau} [\psi_f i_q + (L_d - L_q) i_d i_q] \quad (4)$$

In the above formula, F_{em} is the thrust of the PMLSM, and p_n is the number of pole pairs of the PMLSM, since $L_d = L_q$ in the PMLSM, the thrust equation can be simplified as

$$F_{em} = p_n \frac{3\pi}{2\tau} \psi_f i_q \quad (5)$$

The motion equation of PMLSM is

$$m \frac{dv}{dt} = F_{em} - f_e - Bv \quad (6)$$

In the above formula, m is the mass of the mover in the PMLSM; B is the viscous friction coefficient of the PMLSM and f_e is system disturbance.

3. Active Disturbance Rejection Integrated Controller

3.1. Traditional ADRC

The ADRC usually consists of three parts, divided into TD, extended state observer (ESO), and nonlinear state error feedback control law (NLSEF). The system schematic diagram of the first-order classical ADRC is shown in Figure 2.

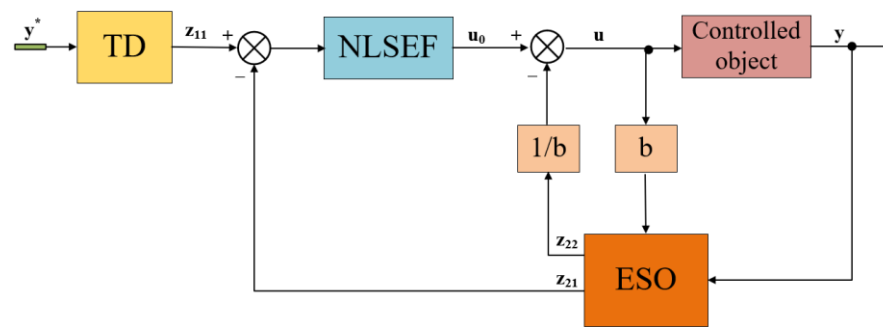


Figure 2. Schematic diagram of first-order classical active disturbance rejection controller.

Set the first-order controlled object in the system to

$$\begin{cases} \dot{x} = f(x, v) + bu \\ y = x \end{cases} \tag{7}$$

The TD model is set up as follows:

$$\begin{cases} e_0 = z_{11} - y^* \\ \dot{z} = -r * fal(e_0, \alpha_0, \delta_0) \end{cases} \tag{8}$$

The ESO model is set as follows:

$$\begin{cases} e_1 = z_{21} - y \\ \dot{z}_{21} = z_{22} - \beta_{01} * fal(e_1, \alpha_1, \delta_1) + bu(t) \\ \dot{z}_{22} = -\beta_{02} * fal(e_1, \alpha_1, \delta_1) \end{cases} \tag{9}$$

The NLSEF model is set up as follows:

$$\begin{cases} e_2 = z_{11} - z_{21} \\ u_0(t) = \beta_1 * fal(e_2, \alpha_2, \delta_2) \\ u(t) = u_0(t) - z_{22}/b \end{cases} \tag{10}$$

In the above formula, x is the state variable; u is the input; y is output; y^* is the expected output; r is the velocity factor; z_{11} and y^* are tracking signals; z_{21} , z_{22} are the state variable of ESO module, z_{21} , z_{22} are the observed value of x and disturbance signal, respectively. β_{01} , β_{02} are the gain of the ESO module; β_1 is the gain of the NLSEF module; z_{22}/b is the compensation quantity used to compensate for multiple disturbances inside and outside the object. The specific meaning of the nonlinear function $fal(e, \alpha, \delta)$ in the above formula is

$$fal(e, \alpha, \delta) = \begin{cases} |e|^\alpha sign(e), & |e| > \delta \\ e/\delta^{1-\alpha}, & |e| \leq \delta \end{cases} \tag{11}$$

The above formula is qualified as $\delta > 0$.

3.2. The Simplified Design of Active Disturbance Rejection Integrated Controller

In the first order ADRC, ten parameters need to be set. In TD, r represents the speed coefficient in the ADRC system, and the tracking speed increases with the increase of the value of r . However, if the value is too large, the overshoot will be large and noise will be quickly introduced. Therefore, the smallest value should be selected on the premise of ensuring the tracking speed during adjustment. The number of adjustable parameters in the first-order ADRC is large and difficult to adjust, so it is difficult to achieve the expected effect in practical application. According to the characteristics of first-order ADRC, a simplified ADRC is proposed in this paper.

Taking the speed loop as an example, there are seven adjustable parameters in the traditional ADRC, α_0 , δ_0 , r , K_p , b , β_{01} , β_{02} respectively. In the simplified ADRC, there

are only three adjustable parameters, K_p , b , p respectively, which is a reduction of four adjustable parameters compared with the traditional ADRC.

The ADRC retains its original performance while reducing adjustable parameters and is applied to the control system of PMLSM.

3.2.1. Design of Active Disturbance Rejection Controller for Velocity Loop

Rewrite the mechanical motion equation of linear motor

$$\dot{v} = f(v, f_e) + bi_q \quad (12)$$

where

$$\begin{cases} f(v, f_e) = -\frac{B}{m}v - \frac{f_e}{m} + bi_q \\ b = \frac{3\pi P_n \Psi_f}{2\tau m} \end{cases} \quad (13)$$

In the first-order active disturbance rejection controller, the TD module is mainly used to extract differential signals and arrange transition processes. However, for the first-order control system, the output of the corresponding second-order ESO module is the observed value of the controlled object and disturbance term, and there is no differential output process. At the same time, the TD module only plays the role of filtering. To simplify the system structure, the TD module is removed, and the nonlinear functions in the ESO module and NLSEF module are replaced by direct errors to reduce the complexity of the system. The simplified velocity loop active disturbance rejection controller is as follows.

Simplify ESO module setup:

$$\begin{cases} \dot{z}_{21} = z_{22} - \beta_{01}(z_{21} - v) + bu \\ \dot{z}_{22} = -\beta_{02}(z_{21} - v) \end{cases} \quad (14)$$

Simplified NLSEF module settings:

$$\begin{cases} u_0 = k_p(v^* - z_{21}) \\ u = u_0 - z_{22}/b \end{cases} \quad (15)$$

According to Formula (15), the simplified ESO module is a standard linear observer, and the poles of the ESO module can be configured using a comprehensive method for linear systems. If $e_1 = z_{21} - v$, $e_2 = z_{22} - f(v, f_e)$, then:

$$\begin{cases} \dot{e}_1 = \dot{z}_{21} - \dot{v} = e_2 - \beta_{01}e_1 \\ \dot{e}_2 = \dot{z}_{22} - \dot{f}(v, f_e) = -\beta_{02} - a(t) \end{cases} \quad (16)$$

where $a(t) = \dot{f}(v, f_e)$

Formula (16) is written in matrix form as

$$\begin{bmatrix} \dot{e}_1 \\ \dot{e}_2 \end{bmatrix} = \begin{bmatrix} -\beta_{01} & 1 \\ -\beta_{02} & 0 \end{bmatrix} \begin{bmatrix} e_1 \\ e_2 \end{bmatrix} + \begin{bmatrix} 0 \\ a(t) \end{bmatrix} \quad (17)$$

The characteristic equation of Formula (17) can be written as

$$p(s) = s^2 + \beta_{01}s + \beta_{02} \quad (18)$$

The conditions for satisfying the above equations for stable operation are $\beta_{01} > 0$ and $\beta_{02} > 0$. If the expected poles of the closed-loop characteristic equation are configured according to the pole assignment method, then

$$p(s) = s^2 + \beta_{01}s + \beta_{02} = s^2 + 2ps + p^2 \quad (19)$$

According to the above formula, $\beta_{01} = 2p$, $\beta_{02} = p^2$, and p is an adjustable parameter, and one parameter that needs to be set in the ESO module is reduced. Generally, the larger p is, the better, but the larger a is, the more the shock will occur, affecting the system's stability.

3.2.2. Design of Active Disturbance Rejection Controller for Current Loop

The q-axis current of the PMLSM can be obtained from Formula (3), in which $-(\pi v i_d)/\tau - (\pi \psi_f v)/\tau L$ is regarded as the disturbance term $w_q(t)$ of the Q-axis current, and can be obtained as

$$\dot{i}_q = -\frac{R_s}{L}i_q + \frac{u_q}{L} + w_q(t) = g(i_q) + w_q(t) + bu \tag{20}$$

On the type, $g(i_q) = -R_s/L$, $b = 1/L$, $u = u_q$. Due to the high requirement of the current loop on the precision of decoupling control, the ESO module and NLSEF module still adopt nonlinear error function, and TD module can still be omitted, so the simplified equation of the first-order current loop active disturbance rejection controller can be obtained.

The ESO module settings are as follows:

$$\begin{cases} e_1 = z_{21} - i_q \\ \dot{z}_{21} = z_{22} - \beta_{01} * fal(e_1, \alpha_1, \delta_1) + g(z_{21}) + bu \\ \dot{z}_{22} = -\beta_{02} * fal(e_1, \alpha_1, \delta_1) \end{cases} \tag{21}$$

The NLSEF module is set as follows:

$$\begin{cases} e_2 = i_q^* - z_{21} \\ u_0 = \beta_1 * fal(e_2, \alpha_2, \delta_2) \\ u = u_0 - (z_{22} + g(z_{21}))/b \end{cases} \tag{22}$$

where i_q^* is the control signal obtained by the current loop, e_1, e_2 are the errors of the q-axis current loop, z_{21} is the tracking signal of i_q , z_{22} is the observed value of the disturbance term $w_q(t)$, u_0 is the control signal output by nonlinear state error feedback control rate, and u is the control signal after disturbance compensation. To sum up, ADRC can be simplified, and the simplified system block diagram is shown in Figure 3.

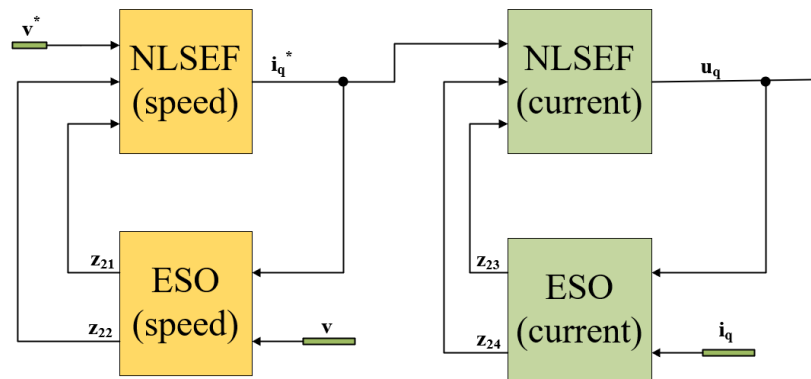


Figure 3. Simplified block diagram of ADRC system.

4. Design of a Non-Singular Terminal SMO

To improve the observation accuracy of the position and velocity information of the linear electric motor observed by an observer, a design combining traditional NFT-SMO and tracking differentiator is proposed in this paper, which can reduce the chattering phenomenon and estimation error of the low-pass filter.

4.1. Non-Singular Fast Terminal Sliding Surface

In the observer, a non-singular fast terminal sliding mode surface with \bar{i} as the state variable is designed, to realize the rapid convergence of the control system within a certain time.

$$s(t) = \bar{i}(t) + p \int_0^t \bar{i}(\tau) d\tau + q \int_0^t |\bar{i}(\tau)|^\lambda \text{sgn}(\bar{i}(\tau)) d\tau \tag{23}$$

In the above formula, $\bar{i} = [\bar{i}_\alpha \quad \bar{i}_\beta]^T$ is the current observation error vector, $p, q > 0$ and $0 < \lambda < 1$, and the meaning of $|\bar{i}(\tau)|^\lambda \text{sgn}(\bar{i}(\tau))$ in the above formula is

$$\text{sgn}(\bar{i}(\tau))|\bar{i}(\tau)|^\lambda = \begin{bmatrix} \text{sgn}(\bar{i}_\alpha(\tau))|\bar{i}_\alpha(\tau)|^\lambda \\ \text{sgn}(\bar{i}_\beta(\tau))|\bar{i}_\beta(\tau)|^\lambda \end{bmatrix} \tag{24}$$

When the control system is in sliding mode, $s = \dot{s} = 0$, the equation can be further rewritten as

$$d\bar{i}/dt = -p\bar{i} - q|\bar{i}|^\lambda \text{sgn}\bar{i} \tag{25}$$

When the control system is in sliding state, the system state will converge to zero in any finite time when the initial state is $\bar{i}(0) \neq 0$. Taking \bar{i}_α as an example, the convergence time of $\bar{i}_\alpha(t_{sa}) = 0$ can be obtained by differential solution of Formula (25):

$$t_{sa} = 1/[p(1 - \lambda)] * \ln[(p|\bar{i}_\alpha(0)|^{1-\lambda} + q)/q] \tag{26}$$

According to Formula (23), in the sliding stage, the non-singular fast terminal sliding mode surface can realize global fast convergence, and there is no negative exponential in \dot{s} , to avoid singular phenomenon and no differential state is required.

4.2. Design of Non-Singular Terminal SMO

The state equation of the PMLSM in the static coordinate system is established as follows, from which the control rate of the SMO is obtained, and the back EMF waveform is further obtained.

$$\begin{cases} \dot{i}_\alpha = \frac{1}{L}(-R_s i_\alpha + u_\alpha - e_\alpha) \\ \dot{i}_\beta = \frac{1}{L}(-R_s i_\beta + u_\beta - e_\beta) \end{cases} \tag{27}$$

In the above formula, $i_\alpha, i_\beta, u_\alpha, u_\beta$ are the stator current and voltage of $\alpha - \beta$ axis, respectively. L is the equivalent inductance of stator winding; e_α, e_β are the back electromotive force of $\alpha - \beta$ axis, and its expression is

$$\begin{cases} e_\alpha = -\psi_f \omega_e \sin \theta_e \\ e_\beta = \psi_f \omega_e \cos \theta_e \end{cases} \tag{28}$$

According to Formula (27), the sliding mode observer equation can be written as

$$\begin{cases} \frac{d\hat{i}_\alpha}{dt} = \frac{1}{L}(-R_s \hat{i}_\alpha + u_\alpha + \sigma_\alpha) \\ \frac{d\hat{i}_\beta}{dt} = \frac{1}{L}(-R_s \hat{i}_\beta + u_\beta + \sigma_\beta) \end{cases} \tag{29}$$

where \hat{i}_α and \hat{i}_β are the observed stator current of $\alpha - \beta$ axis; σ_α and σ_β are sliding mode control laws. By finding the difference between Formulas (27) and (29) and transforming, the current error system can be obtained as:

$$\frac{d\bar{i}}{dt} = \frac{1}{L}(-R_s \bar{i} + e + \sigma) \tag{30}$$

In the above formula, $\bar{i} = [\bar{i}_\alpha \quad \bar{i}_\beta]^T$ is the observation error of the SMO for the current, where $\bar{i}_\alpha = \hat{i}_\alpha - i_\alpha$ and $\bar{i}_\beta = \hat{i}_\beta - i_\beta$ are the error between the observed current value

and the actual current value. Applying the sliding mode surface shown in Formula (23) to the current error system shown in Formula (30), the control law of SMO can be obtained as

$$\begin{cases} \sigma = \sigma_{eq} + \sigma_{sw} \\ \sigma_{eq} = R_s \bar{i} - L * (p\bar{i} + q|\bar{i}|^\lambda \operatorname{sgn}\bar{i}) \\ \sigma_{sw} = -k|s|^\gamma \operatorname{sgns} - \eta s \end{cases} \quad (31)$$

where $|s|^\gamma = [|s_\alpha|^\gamma \quad |s_\beta|^\gamma]^T$, $k, \eta > 0$, $0 < \gamma < 1$. In the sliding mode control law represented by Formula (31), σ_{eq} is obtained by $\dot{s} = 0$ and ignoring the back electromotive force, and the terminal attractor $k|s|^\gamma \operatorname{sgns}$ constitutes the switching function in σ_{sw} , so $k\operatorname{sgns}$ to reduce the chattering phenomenon caused by the switching function ηs in the traditional SMO. At the same time, the approaching rate of the control system when it is far from the sliding mode surface is guaranteed by the item in the above equation. Since the state indices shown in Formula (31) are all greater than zero, the constructed SMO is non-singular.

4.3. Stability Analysis

To verify the stability of the overall design of the NFT-SMO, the Lyapunov function is chosen for stability analysis

$$V = s^T s / 2 \quad (32)$$

The derivative of V is obtained by substituting Equations (23), (30), and (31) into (32)

$$\begin{aligned} \dot{V} &= s^T \dot{s} = s^T (d\bar{i}/dt + p\bar{i} + q|\bar{i}|^\lambda \operatorname{sgn}\bar{i}) \\ &= s^T [(-R_s \bar{i} + e + \sigma) / L + p\bar{i} + q|\bar{i}|^\lambda \operatorname{sgn}\bar{i}] \\ &= s^T (e - k|s|^\gamma \operatorname{sgns} - \eta s) / L \\ &= (s_\alpha e_\alpha + s_\beta e_\beta - k|s_\alpha|^{\gamma+1} - k|s_\beta|^{\gamma+1} - \eta s_\alpha^2 - \eta s_\beta^2) / L \end{aligned} \quad (33)$$

Additionally, meet

$$\begin{aligned} \dot{V} &= (s_\alpha e_\alpha + s_\beta e_\beta - k|s_\alpha|^{\gamma+1} - k|s_\beta|^{\gamma+1} - \eta s_\alpha^2 - \eta s_\beta^2) / L \\ &\leq (|s_\alpha| |e_\alpha| + |s_\beta| |e_\beta| - k|s_\alpha|^{\gamma+1} - k|s_\beta|^{\gamma+1} - \eta s_\alpha^2 - \eta s_\beta^2) / L \end{aligned} \quad (34)$$

\dot{V} is negative definite when it's outside the condition $\{|s_x| \leq \min((|e_x|/k)^{1/\gamma}, |e_x|/\eta), x = \alpha, \beta\}$. For $c > (\min((|e_x|/k)^{1/\gamma}, |e_x|/\eta))^2 / 2$, the solution starting from $(V \leq c)$ always remains within it at future moments, where e_x is the actual counter electromotive force. Since \dot{V} is negative on the boundary $V = c$, the solutions to the above equations are uniformly bounded.

4.4. Track Differentiator Settings

In this paper, a low chattering fast tracker with terminal attractor is designed to achieve high precision tracking of the back electromotive force, further reduce the high-frequency noise, and have the function of filtering:

$$\begin{cases} \dot{z}_1 = z_2 \\ \dot{z}_2 = -aR^2(z_1 - \varepsilon_x + z_2/R) - \\ \quad bR^2 \left[(z_1 - \varepsilon_x)^m \operatorname{sgn}(z_1 - \varepsilon_x) + \left(\frac{z_2}{R}\right)^m \operatorname{sgn}z_2 \right] \end{cases} \quad (35)$$

In the above formula, $R, a, b > 0$ and $m > 1$; R is the time scale, reflecting the total speed of the overall sense; a and b are the specific gravity of linear factor and nonlinear factor, and also represent the tracking rate when the distance between them and the equilibrium point is far and close. z_1 and z_2 are the state variables of the tracking dif-

ferentiator; $\varepsilon_x(x = \alpha, \beta)$ is the input variable, which is the tracking target of the tracking differentiator. z_1 realizes high-precision tracking of ε_x , and realizes filtering function of ε_x because z_1 is obtained by integration twice. Compared with the traditional LPF, the tracking differentiator reduces the phase problem caused by the LPF by adjusting the tracking rate while keeping the amplitude of the back EMF unchanged. The structure of NFT-SMO combined with a tracking differentiator is shown in Figure 4.

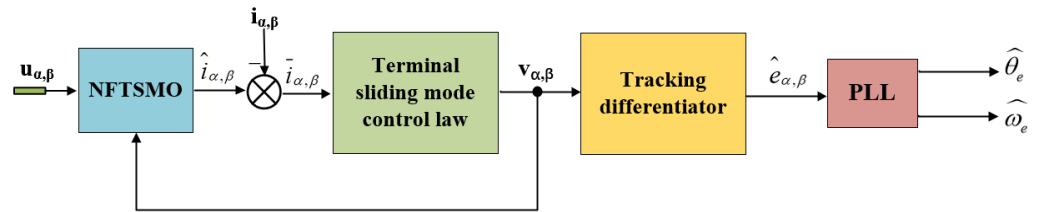


Figure 4. Structure diagram of the novel NFT-SMO.

4.5. PLL Policy Application

The sliding mode control has fluctuations in the sliding mode, and there will be chattering in the back EMF observed by the observer. Therefore, the PLL system is used to extract the rotor position information. The schematic diagram of the PLL structure is shown in Figure 5.

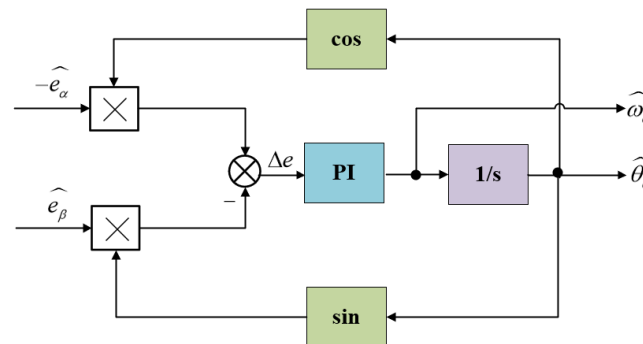


Figure 5. PPL structure diagram.

Set

$$k = (L_d - L_q)(\omega_e i_d - p i_q) + \hat{\omega}_e \psi_f \tag{36}$$

Since $L_d = L_q$ in the PMLSM, the above equation can be simplified as:

$$k = \hat{\omega}_e \psi_f \tag{37}$$

In the traditional phase-locked link, its position error signal is:

$$\begin{aligned} \Delta e &= -e_\alpha \cos \hat{\theta}_e - e_\beta \sin \hat{\theta}_e \\ &= k \sin \theta_e \cos \hat{\theta}_e - k \cos \theta_e \sin \hat{\theta}_e \\ &= k \sin(\theta_e - \hat{\theta}_e) \end{aligned} \tag{38}$$

When the system approaches the steady state, the value of $|\theta_e - \hat{\theta}_e|$ is minimal. Assume that $\sin(\theta_e - \hat{\theta}_e) = \theta_e - \hat{\theta}_e$, and after normalization, the position signal error is

$$\Delta \bar{e} = \frac{\Delta e}{\sqrt{e_\alpha^2 + e_\beta^2}} = \frac{k(\theta_e - \hat{\theta}_e)}{\sqrt{e_\alpha^2 + e_\beta^2}} = \theta_e - \hat{\theta}_e \tag{39}$$

Therefore, the PLL closed-loop transfer function from $\hat{\theta}_e$ to θ_e is:

$$G(s) = \frac{\hat{\theta}_e}{\theta_e} = \frac{2\xi\omega_n s + \omega_n^2}{s^2 + 2\xi\omega_n s + \omega_n^2} \tag{40}$$

where $\xi = \sqrt{k/k_i}$, $\omega_n = (k_p/2)\sqrt{k/k_i}$. ω_n determines the bandwidth of the PI regulator, k_p and k_i are normal numbers.

5. Simulation and Experimental Results

5.1. Simulation

The block diagram of the sensorless vector control system of PMLSM designed in this paper is set up in MATLAB/SIMULINK, as shown in Figure 6. In addition, the traditional PI control system and sliding mode control (SMC) system were set up to compare the control effect, and the NFT-SMO without the tracking differentiator was set up to compare with the NFT-SMO with the tracking differentiator. The simulation model is established according to the motor driving parameters shown in Table 1. The feasibility and effectiveness of the PMLSM control system designed in this paper are verified by simulation and experiment.

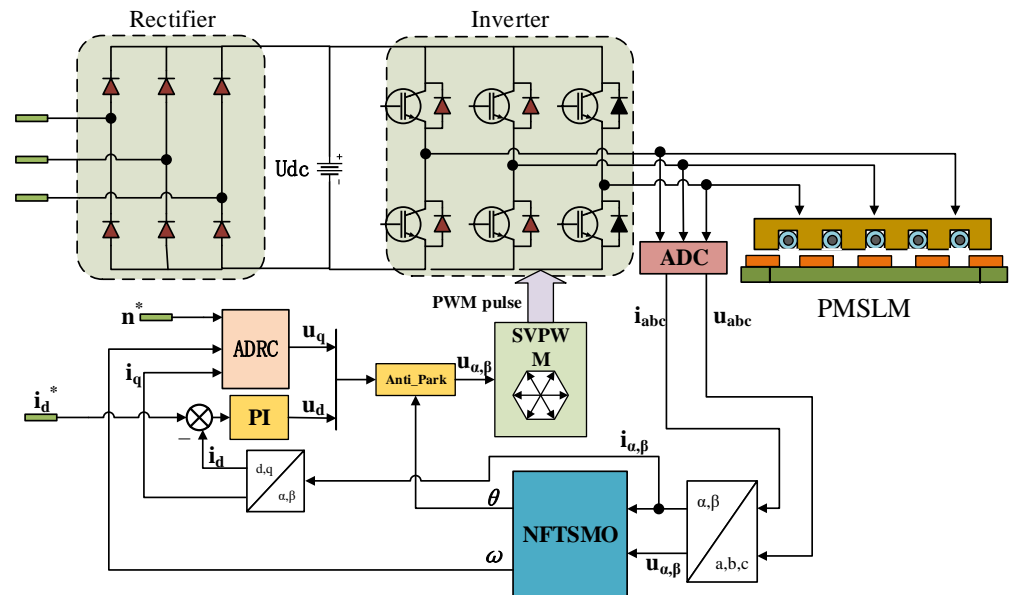


Figure 6. Control system block diagram of PMLSM.

Table 1. Main parameters of motor.

Parameter	Value
stator resistance R_s/Ω	4.0
d-q axis inductance L_{dq}/mH	8.2
Mover mass m/kg	1.425
Viscous friction coefficient $B/N/m \cdot s$	44
Polar distance τ/m	0.016
DC Bus Voltage U/V	200

In this paper, the ADRC parameters of the speed loop and current loop are adjusted by the empirical setting method as follows:

Speed loop: $K_p = 500$, $b = 200$, $p = 500$, $\beta_{01} = 2p = 1000$, $\beta_{02} = p^2 = 250,000$.

Current loop: $\beta_1 = 2000$, $b = 200$, $\alpha_1 = 1.2$, $\delta_1 = 0.01$, $\beta_{01} = 8500$, $\beta_{02} = 4250^2$.

To verify that the adjustable parameter p cannot be too large, $p = 500$ and $p = 1000$ are selected for comparison and verification. The speed waveforms of the two control systems are shown in Figure 7. It can be seen from Figure 7 that when $p = 1000$, the response time

of the speed waveform of the system is fast, but the jitter is large in the first 0.5 s, and the maximum buffeting amplitude is 2.58 m/s at 0.0075 s. When $p = 500$, the overall speed waveform of the system is relatively stable and the jitter is small. The buffeting amplitude reaches the maximum value of 1.38 m/s at 0.03 s. It is obvious that when p is increased, the response time of the velocity waveform is faster, but at the same time, it will produce large buffeting and fluctuation. Therefore, it is necessary to take an appropriate value of p to achieve a better control effect.

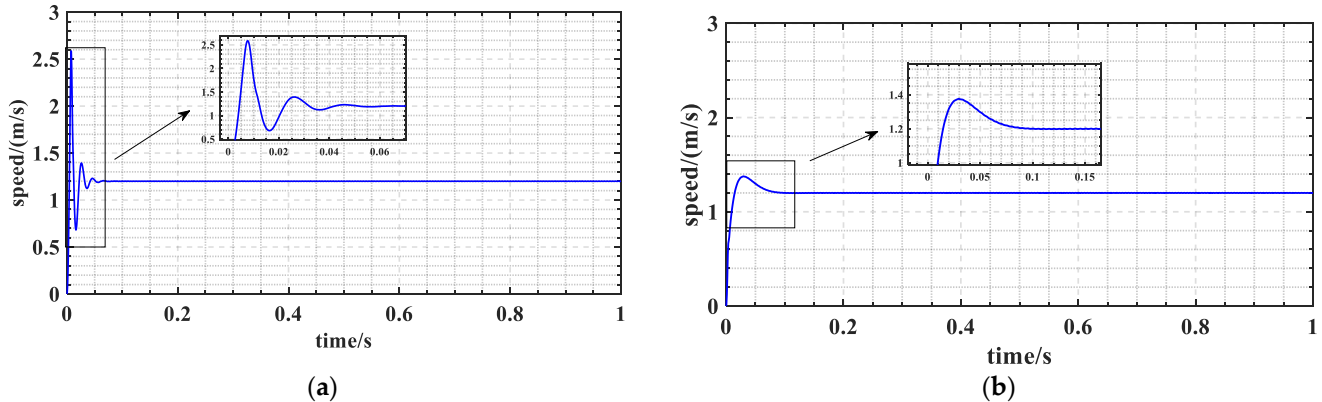


Figure 7. Velocity waveforms at different p values. (a) $p = 1000$, (b) $p = 500$.

To facilitate the analysis of the dynamic performance of the control system, the traditional PI control system, the traditional SMC control system and the proposed ADRC control system was built in this paper. The given speed of the system was set as $(1 \text{ m/s}^{-2} \text{ m/s}^{-3} \text{ m/s})$, and the control effect of the three systems under the step speed was compared.

Figure 8 shows three control strategies. PI control system and ADRC control system have less overshoot and adjustment time in three acceleration stages than conventional SMC control systems. In the stage of steady speed operation, the part as shown in Figure 8 is captured for magnification observation. In the stage of steady speed operation, the control effect of the traditional SMC control system is the worst, followed by the PI control system, and the jitter of the ADRC control system is the least.

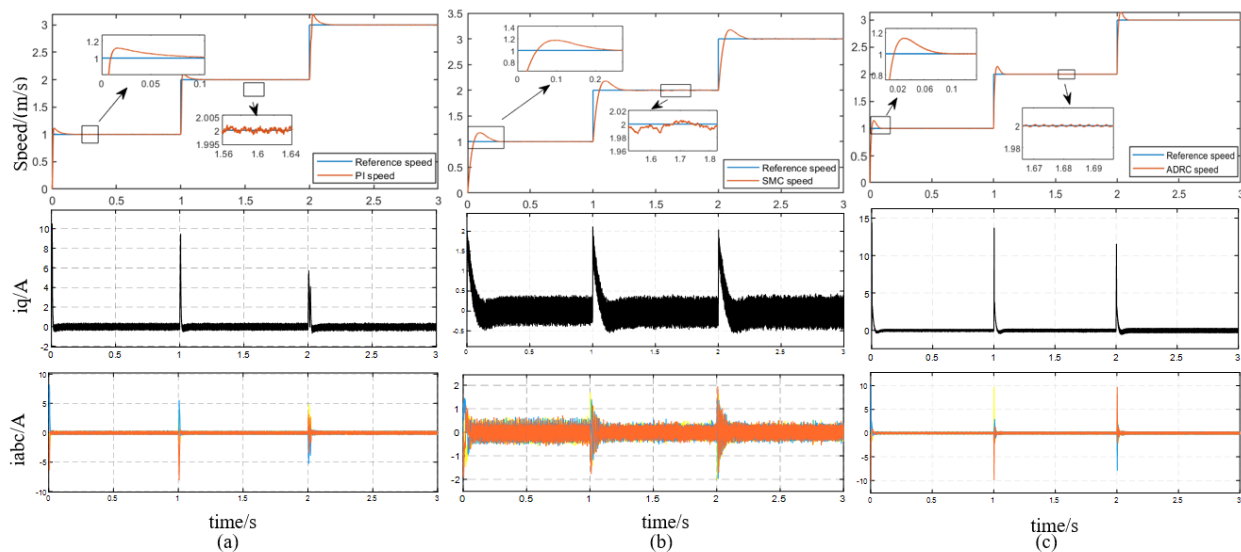


Figure 8. Simulation results of reference velocity step change under three different control strategies. Top to bottom: speed contrast, Q axis current, three-phase current. (a) traditional PI control; (b) traditional SMC control; (c) proposed ADRC control.

A more complex speed tracking was added to the system. Given the speed of the system was the reference sine curve shown in the blue line in Figure 9. All three control strategies could track the given speed curve with sine changes. PI and ADRC control systems can stably track a given speed. Three regions as shown in Figure 9 are selected for local amplification. It can be seen that ADRC is more accurate than PI tracking in the three local amplification images.

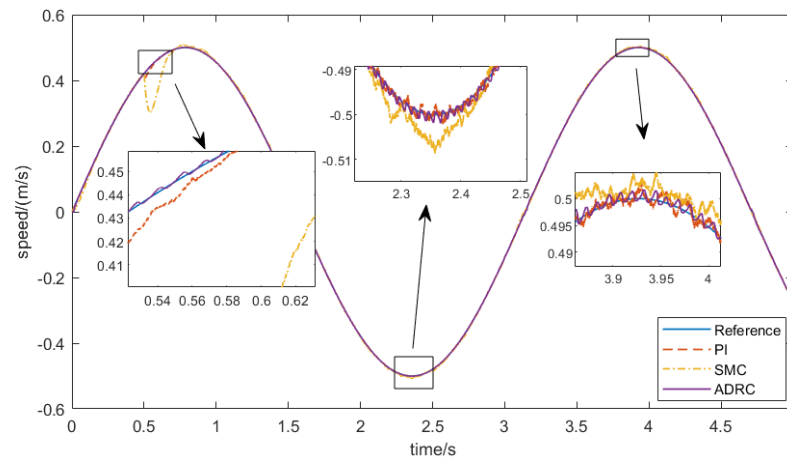


Figure 9. Velocity tracking curve of sinusoidal change of reference velocity under three different control strategies.

Add random load as shown in Figure 10 to the system and observe the operation of the system to analyze the anti-disturbance ability of the system. Figure 11 shows the comparison of the running speeds of the three control systems with random loads when the system speed is given at 1.5 m/s. Among the three control strategies, traditional SMC control has the worst effect. The proposed ADRC control system has the lowest velocity fluctuation when the velocity reaches a given speed.

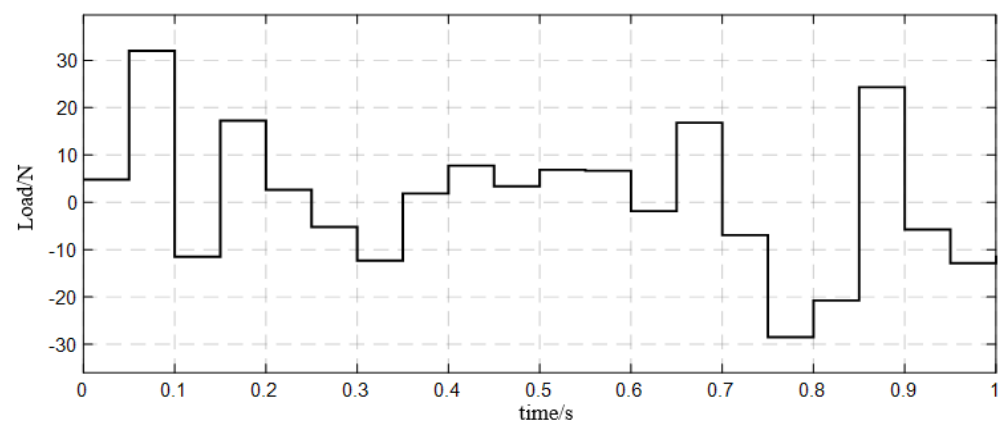


Figure 10. Random load added to the control system.

After verifying the excellent control performance of the designed ADRC, the NFT-SMO is built and compared with the NFT-SMO with the differential tracker (TD). The given speed of the system is a step change, and the given speed is 1 m/s^{-2} m/s^{-3} m/s . The speed tracking down the three observers and PMLSM is compared.

In Figure 12, the error between the observed velocity and the real velocity of the control system without TD is about 0.2. With the addition of TD, the error between the observed velocity and the real velocity of the NFT-SMO is 0.08, and the accuracy is improved by 60%. The effectiveness of the designed control system is verified by simulation.

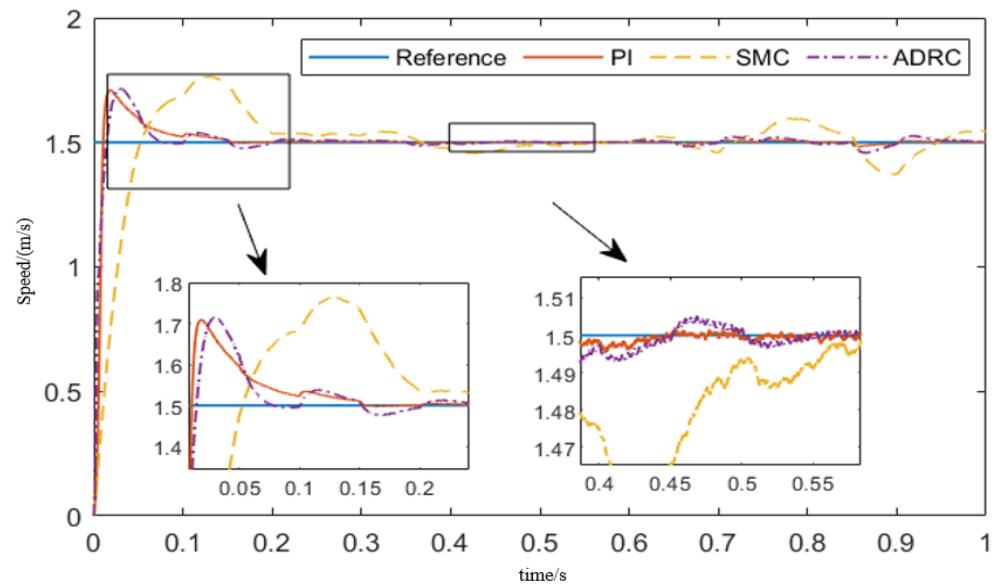


Figure 11. Comparison of running speed.

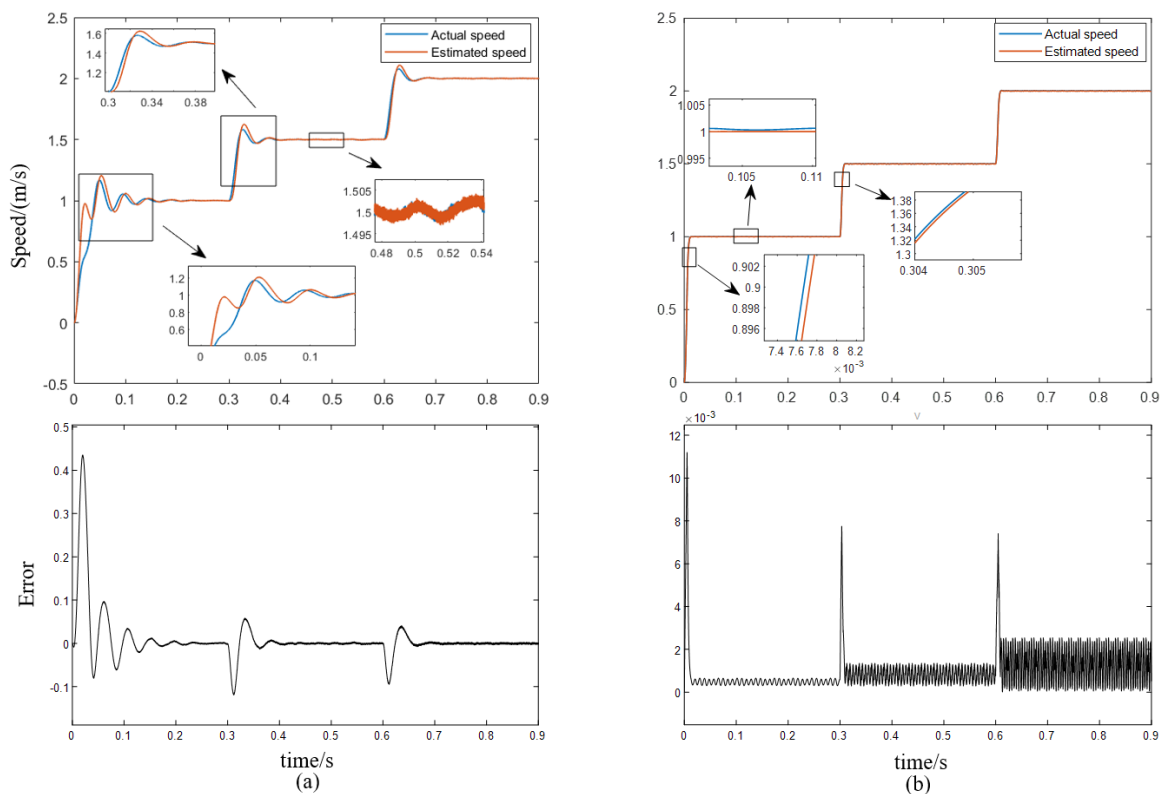


Figure 12. Control effects of two different controllers under-speed step changes. From top to bottom: the difference between the actual velocity and the estimated velocity observed by the observer. (a) NFT-SMO; (b) NFT-SMO with TD.

5.2. Experiment

Compared with the simulation environment, the experimental environment has more disturbances from the outside, and there is heating phenomenon in the operation of the electricity. Building the experimental platform for verification is conducive to further improving the control system and making the designed algorithm better and faster in practical application. This paper sets up the experimental platform as shown in Figures 13 and 14. PMLSM control driver schematic diagram is shown in Figure 15. Experimental verification is carried

out using STM32 and Matlab automatic code generation tool. Using STM32CubeMX software to generate the underlying configuration code and further optimize the settings can enable developers to focus on algorithm implementation and improving work efficiency. The code generation tool generates the control algorithm code and connects it to the STM32 kernel code configuration by STM32CUBE. The compiled code is downloaded to STM32 for further improvement and parameter debugging. The ADC module and timer module obtain the electrical signal and position signal of the PMLSM through the hall sensor and micro-grid encoder, respectively. The encoder is used to compare with the observer designed in this paper. The PMLSM parameters selected in this paper are shown in Table 1.

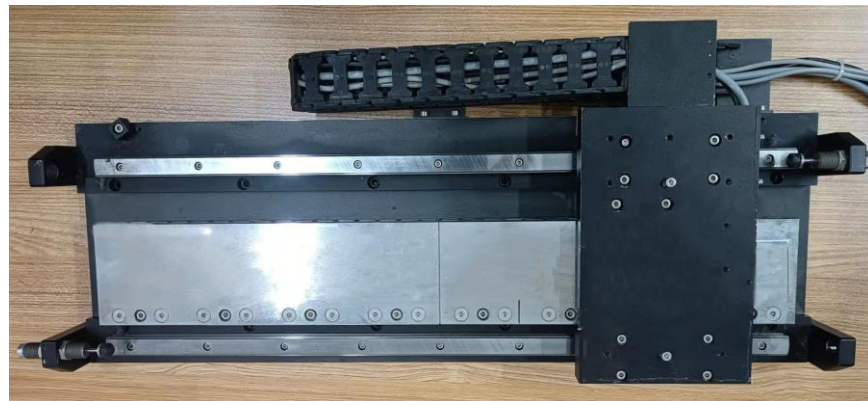


Figure 13. PMLSM.

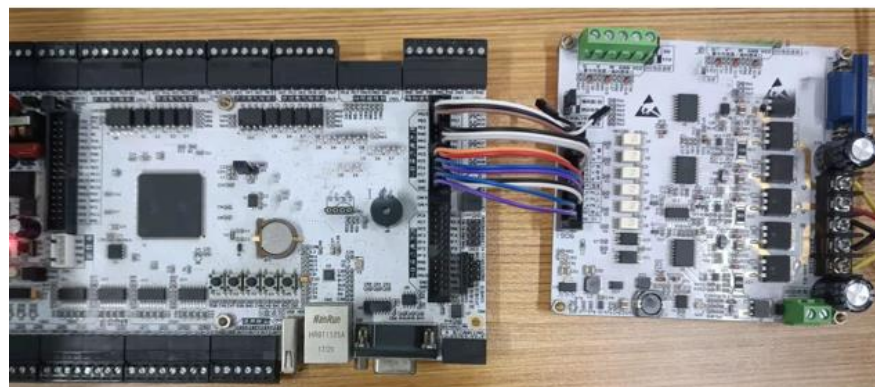


Figure 14. Control and drive circuit.

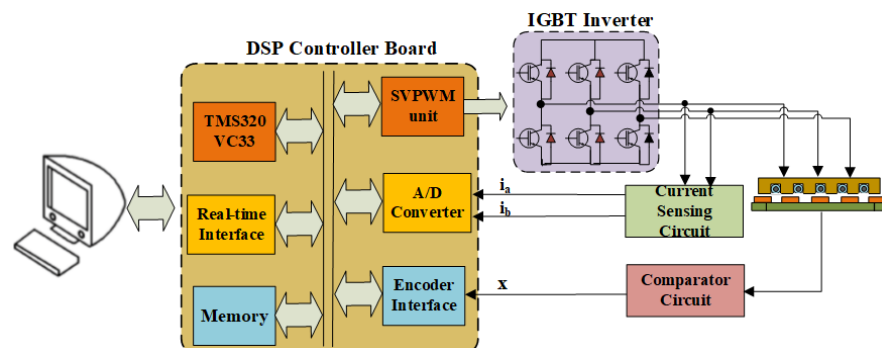


Figure 15. Schematic diagram of the PMLSM drive control system.

In the following experiments, the traditional PI control, the traditional SMC system, and the proposed ADRC system are implemented. In the experiment, in order to better test the dynamic performance of the control system, the given speed of the system is set to 1 m/s~2 m/s. Figure 16 shows the running speed of the system after a given speed, as well

as the comparison of the overshoot, adjustment time, and static error of the three systems. It can be seen from Figure 16 that the overshoot of the PI control system in the two motion stages is 15.1% and 15.3%, the adjustment time is 0.081 s and 0.077 s, and the fluctuation range of the static error is 0.013 m and 0.016 m. The overshoot of the traditional SMC system in the two motion stages is 22.3% and 22.6%, the adjustment time is 0.231 s and 0.228 s, and the fluctuation range of the static error is 0.024 m and 0.026 m. The overshoot of the ADRC system in the two motion stages is 10% and 11.3%, the adjustment time is 0.113 s and 0.118 s, and the fluctuation range of the static error is 0.008 m and 0.006 m. It can be seen from Figure 16 that the ADRC system in this paper has smaller overshoot and static error than the PI control system and the SMC system, which reflects the strong anti-interference and high control accuracy of the ADRC system.

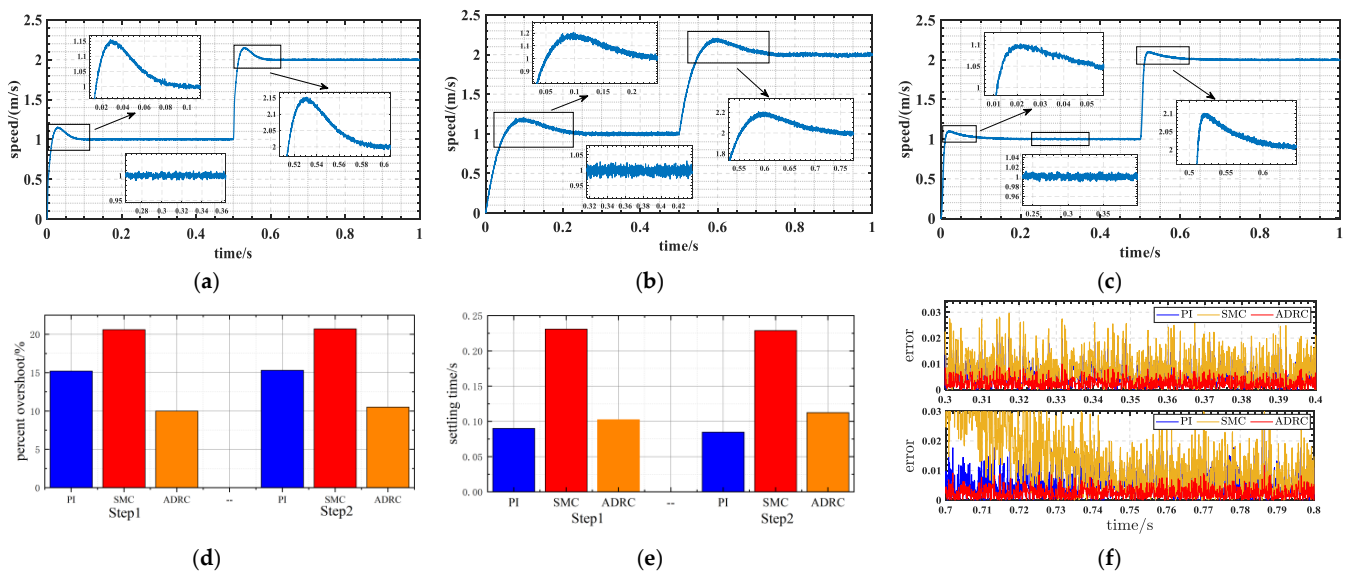


Figure 16. Comparison of velocity waveforms under three control strategies. (a) The running speed of the PI control system. (b) The running speed of the SMC system. (c) The running speed of the ADRC system. (d) Comparison of overshoot of three control systems. (e) Comparison of adjustment time of three control systems. (f) Comparison of static errors of three control systems.

Figure 17 shows that when the given speed of the system is set to 1.2 m/s, and when the system runs to 0.4 s, the on-off controllable solenoid valve is controlled to complete the loading action, and the performance of the control system is analyzed through the anti-interference ability and dynamic adjustment ability. The operating speed is greatly affected when using the traditional SMC system, and it takes the longest time to recover from the normal operating speed. The traditional PI control strategy and the ADRC control strategy proposed in this paper have similar effects on the system after adding disturbance, but the ADRC system has a relatively small overshoot and strong anti-interference ability.

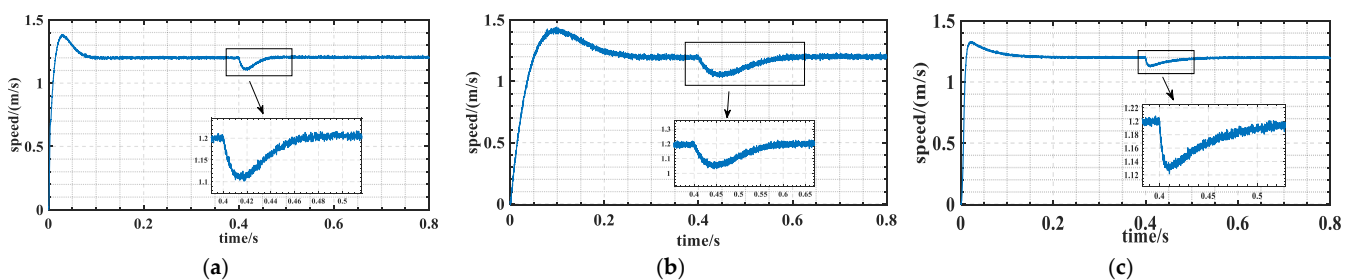


Figure 17. The speed waveform comparison of the three systems after loading. (a) Velocity waveform of PI control system after adding load. (b) Velocity waveform of SMC system after adding load. (c) Velocity waveform of ADRC system after adding load.

After verifying the good dynamic performance of the improved ADRC control proposed in this paper, the effectiveness of the novel NFTSMO is analyzed by comparing NFTSMO without TD and NFTSMO with TD. In this paper, the velocity-related numerical points observed by the traditional NFTSMO, the novel NFTSMO, and the mechanical sensor are imported into the computer to draw the waveform diagram. In Figure 18, the waveform diagrams with and without the observer are compared, and the jitter amplitude of the traditional NFTSMO and the novel NFTSMO as well as the error relative to the mechanical sensor can be clearly obtained. As shown in Figure 18, the observer tracking performance of PMLSM from the stationary speed to the given speed was analyzed at a given system speed of 1.5 m/s. The jitter amplitude of the observed effect of the NFTSMO without the TD is 10% of the given speed. The jitter of the observer with TD is 5.3% of the given speed.

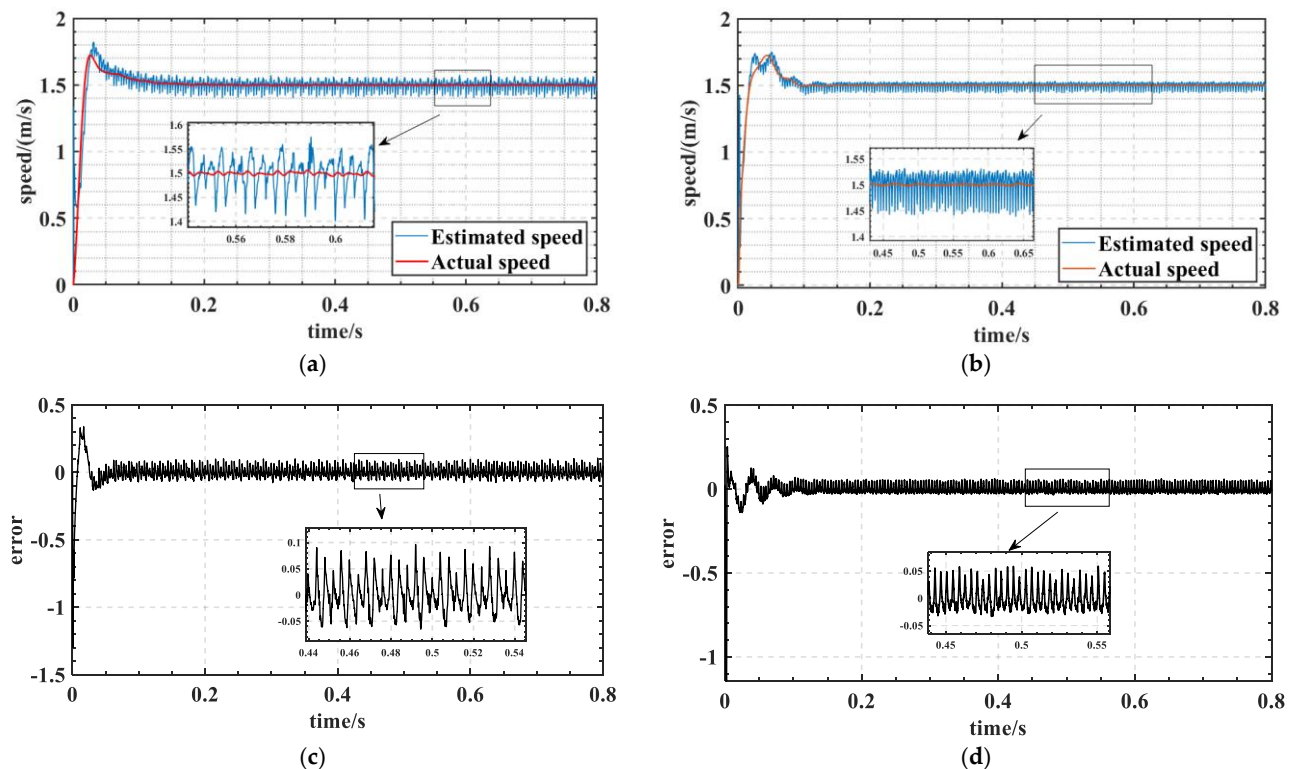


Figure 18. Comparison of the two observers. (a) Comparison of the observed speed of traditional NFTSMO with the actual speed. (b) Comparison of the observed speed of novel NFTSMO with the actual speed. (c) Observation error of traditional NFTSMO. (d) Observation error of novel NFTSMO.

6. Conclusions

In an attempt to solve the problems of the many traditional ADRC parameters, unclear meaning, and difficulty of adjustment, and to accurately estimate the mover position and speed required by the position free vector control system of PMLSM, an improved ADRC and a novel NFTSMO based on TD are proposed. The ADRC is simplified by removing the TD module in ADRC and replacing the nonlinear function in ESO and NLSEF modules with direct error. At the same time, TD is added to the traditional NFTSMO to obtain a smooth back EMF, reduce the phase lag caused by LPF in the traditional SMO, and modulate the actuator position and speed information from the observed back EMF based on the PLL principle. In the simulation and experiment, ADRC is compared with the PI controller and SMC. Through the comparison of overshoot, adjustment time, and static error, ADRC in this design has strong anti-interference and a fast response speed while simplifying the structure. At the same time, the speed waveform observed by traditional NFTSMO and novel NFTSMO is compared with that observed by mechanical sensors. The comparison of buffeting amplitude and error shows that the novel NFTSMO has the advantages of fast

convergence speed, high tracking accuracy, small back EMF buffeting, and good system stability. Through the simulation and experimental platform, it is fully verified that the control strategy can not only simplify the structure of the system but also improve the control performance of the control system in the sensorless state.

Author Contributions: Writing—review and editing, supervision, project administration, funding acquisition, Z.L.; review and editing, supervision, project administration, funding acquisition, H.S. (Z.L. and H.S. contributed equally to this work as co-correspondent author); methodology, software, writing—original draft preparation, J.W. and Z.Z.; validation, S.W. and X.C. All authors have read and agreed to the published version of the manuscript.

Funding: This work is supported by the National Natural Science Foundation of China (No. 51877070, U20A20198, 51577048), the Natural Science Foundation of Hebei Province of China (No. E2021208008), the Talent Engineering Training Support Project of Hebei Province (A201905008), the National Engineering Laboratory of Energy-saving Motor & Control Technique, Anhui University (No. KFKT201901).

Conflicts of Interest: The authors declare no conflict of interest.

References

1. Yang, R.; Li, L.; Wang, M.; Zhang, C. Force Ripple Compensation and Robust Predictive Current Control of PMLSM Using Augmented Generalized Proportional–Integral Observer. *IEEE J. Emerg. Sel. Top. Power Electron.* **2021**, *9*, 302–315. [[CrossRef](#)]
2. Dong, F.; Zhao, J.; Zhao, J.; Song, J.; Chen, J.; Zheng, Z. Robust Optimization of PMSLM Based on a New Filled Function Algorithm With a Sigma Level Stability Convergence Criterion. *IEEE Trans. Ind. Inform.* **2021**, *17*, 4743–4754. [[CrossRef](#)]
3. Yang, R.; Wang, M.; Li, L.; Wang, G.; Zhong, C. Robust Predictive Current Control of PMSLM With Extended State Modeling Based Kalman Filter: For Time-Varying Disturbance Rejection. *IEEE Trans. Power Electron.* **2020**, *35*, 2208–2221. [[CrossRef](#)]
4. Cui, F.; Sun, Z.; Xu, W.; Qian, H.; Cao, C. Optimization Analysis of Long Primary Permanent Magnet Linear Synchronous Motor. *IEEE Trans. Appl. Supercond.* **2021**, *31*, 1–4. [[CrossRef](#)]
5. Zhao, J.; Mou, Q.; Zhu, C.; Chen, Z.; Li, J. Study on a Double-Sided Permanent-Magnet Linear Synchronous Motor With Reversed Slots. *IEEE/ASME Trans. Mechatron.* **2021**, *26*, 3–12. [[CrossRef](#)]
6. Liu, Y.; Gao, J.; Zhong, Y.; Zhang, L. Extended State Observer-Based IMC-PID Tracking Control of PMSLM Servo Systems. *IEEE Access* **2021**, *9*, 29036–49046.
7. Hamed, H.A.; El-Barbary, Z.; Moursi, M.S.; Chamarthi, P.K. A New δ -MRAS Method For Motor Speed Estimation. *IEEE Trans. Power Deliv.* **2020**, *36*, 1903–1906. [[CrossRef](#)]
8. Xu, W.; Junejo, A.K.; Tang, Y.; Shahab, M.; Habib, H.U.R.; Liu, Y.; Huang, S. Composite Speed Control of PMSM Drive System Based on Finite Time Sliding Mode Observer. *IEEE Access* **2021**, *9*, 151803–151813. [[CrossRef](#)]
9. Hao, Z.; Yang, Y.; Gong, Y.; Hao, Z.; Zhang, C.; Song, H.; Zhang, J. Linear/Nonlinear Active Disturbance Rejection Switching Control for Permanent Magnet Synchronous Motors. *IEEE Trans. Power Electron.* **2021**, *36*, 9334–9347. [[CrossRef](#)]
10. Zuo, Y.; Mei, J.; Jiang, C.; Yuan, X.; Xie, S.; Lee, C.H.T. Linear Active Disturbance Rejection Controllers for PMSM Speed Regulation System Considering the Speed Filter. *IEEE Trans. Power Electron.* **2021**, *36*, 14579–14592. [[CrossRef](#)]
11. Lin, P.; Wu, Z.; Liu, K.-Z.; Sun, X.-M. A Class of Linear–Nonlinear Switching Active Disturbance Rejection Speed and Current Controllers for PMSM. *IEEE Trans. Power Electron.* **2021**, *36*, 14366–14382. [[CrossRef](#)]
12. Chen, S.; Zhao, Y.; Qiu, H.; Ren, X. High-Precision Rotor Position Correction Strategy for High-Speed Permanent Magnet Synchronous Motor Based on Resolver. *IEEE Trans. Power Electron.* **2020**, *35*, 9716–9726. [[CrossRef](#)]
13. Colombo, L.; Corradini, M.L.; Cristofaro, A.; Ippoliti, G.; Orlando, G. An Embedded Strategy for Online Identification of PMSM Parameters and Sensorless Control. *IEEE Trans. Control Syst. Technol.* **2019**, *27*, 2444–2452. [[CrossRef](#)]
14. de Castro, A.G.; Guazzelli, P.R.U.; de Oliveira, C.M.R.; Pereira, W.C.D.A.; de Paula, G.T.; Monteiro, J.R.B.D.A. Optimized Current Waveform for Torque Ripple Mitigation and MTPA Operation of PMSM with Back EMF Harmonics based on Genetic Algorithm and Artificial Neural Network. *IEEE Lat. Am. Trans.* **2020**, *9*, 1646–1655. [[CrossRef](#)]
15. Du, B.; Zhao, T.; Han, S.; Song, L.; Cui, S. Sensorless Control Strategy for IPMSM to Reduce Audible Noise by Variable Frequency Current Injection. *IEEE Trans. Ind. Electron.* **2020**, *67*, 1149–1159. [[CrossRef](#)]
16. Cheng, H.; Sun, S.; Zhou, X.; Shao, D.; Mi, S.; Hu, Y. Sensorless DPCC of PMLSM Using SOGI-PLL-Based High-Order SMO With Cogging Force Feedforward Compensation. *IEEE Trans. Transp. Electrification.* **2022**, *8*, 1094–1104. [[CrossRef](#)]
17. Li, Z.; Zhou, S.; Xiao, Y.; Wang, L. Sensorless Vector Control of Permanent Magnet Synchronous Linear Motor Based on Self-Adaptive Super-Twisting Sliding Mode Controller. *IEEE Access* **2019**, *7*, 44998–45011. [[CrossRef](#)]
18. Xu, B.; Zhang, L.; Ji, W. Improved Non-Singular Fast Terminal Sliding Mode Control With Disturbance Observer for PMSM Drives. *IEEE Trans. Transp. Electrification.* **2021**, *7*, 2753–2762. [[CrossRef](#)]

19. Fu, D.; Zhao, X.; Zhu, J. A Novel Robust Super-Twisting Nonsingular Terminal Sliding Mode Controller for Permanent Magnet Linear Synchronous Motors. *IEEE Trans. Power Electron.* **2022**, *37*, 2936–2945. [[CrossRef](#)]
20. Shao, K.; Zheng, J.; Huang, K.; Wang, H.; Man, Z.; Fu, M. Finite-Time Control of a Linear Motor Positioner Using Adaptive Recursive Terminal Sliding Mode. *IEEE Trans. Ind. Electron.* **2020**, *67*, 6659–6668. [[CrossRef](#)]